Contents lists available at ScienceDirect

Comptes Rendus Mecanique

Computational modeling of material forming processes / Simulation numérique des procédés de mise en forme

A microscale finite element model for joining of metals by large plastic deformations

Kavan Khaledi *, Shahed Rezaei, Stephan Wulfinghoff, Stefanie Reese

Institute of Applied Mechanics, RWTH Aachen University, 52074 Aachen, Germany

A R T I C L E   I N F O

A B S T R A C T

The paper aims to present a finite element model for the bonding process of metals at the microscale. To accomplish this, first, the mechanism of joining by plastic deformation at the microscopic level is explained. Then, based on the film theory of bonding, a finite element model is developed, which enables to simulate the bonding process between metallic layers subjected to large plastic deformation. The model presented in this paper takes into account the most important physical micro-mechanisms taking place during the bond formation process, i.e. (1) the breakage of the brittle oxide layer above the metallic surfaces, (2) the decohesion process occurring between the oxide layer and the metal substrate, (3) the extrusion of the substrate into the created cracks under large plastic deformations, and (4) the bond formation in between the fractured oxide layers. In addition, an extended version of a cohesive zone model is proposed to describe the bond formation between the metal surfaces. Finally, it is shown that the model can be used to provide a description regarding bond strength evolution. In this context, the effects of influencing factors, such as the degree of deformation and the thickness of the oxide layer, are numerically investigated. The presented finite element model can be regarded as a useful tool to characterize the key factors in joining processes such as roll bonding and cold forging.

© 2018 Académie des sciences. Published by Elsevier Masson SAS. All rights reserved.

1. Introduction

Joining by plastic deformation can be regarded as a solid-state welding process, in which two metallic surfaces are joined together using a relatively high normal pressure at a temperature below the melting point. In the absence of oxidation, if two smooth and corrosion-free metallic surfaces are intensively pressed together, the metal crystal grains join each other along the interface and create metallurgical bonding. However, in atmospheric conditions, the metallic surfaces are always covered by a thin layer of oxide and of other contaminants. In this case, the oxide film is a barrier to bond formation. Unlike the metal substrate, which exhibits ductile behavior, the oxide layer is of brittle nature. Therefore, it breaks up under large plastic deformation. In this way, the virgin metal can extrude into the channels created due to the fracturing of the brittle layer. Then, the two opposing substrates come into contact, and metallurgical bonding is established between them. In general, the mechanism of joining by plastic deformation is well described by the so-called "film theory" of bonding [1]. During the recent years, a number of studies have been conducted in an attempt to describe the mechanism of bond
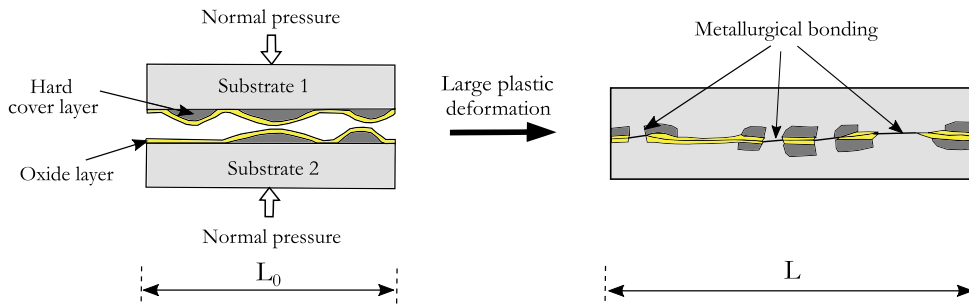

Fig. 1. Schematic representation of the bonding process based on film theory [7].

formation for metals. Among them, the models proposed by Zhang and Bay (1997) [2] and Cooper and Allwood (2014) [3] are especially worth to be mentioned. In each of these studies, first, the micro-mechanisms of bonding were simplified. Then, an analytical model was developed to predict bond strength evolution. On the other hand, only a few authors have used the finite element method to investigate the process of bond formation. Recently, Bambach et al. (2014) [4] have proposed a finite element framework for the evolution of bond strength in cold welding processes. In this framework, the bonding model of Zhang and Bay (1997) [2,5] was implemented into a contact subroutine of ABAQUS/Standard to describe the joining in cold roll-bonding processes. In the same line of thought, Kebriaei et al. (2014) [6] proposed a bonding interface element in ABAQUS/Standard based on the cohesive zone modeling technique. However, both studies were specifically performed to describe the bond formation process at the macroscale. The purpose of this paper is twofold, as follows.

- A finite element model is developed to describe the metal bonding process at the microscale. The model accounts for the most important micro-mechanisms occurring during the bond formation process. Moreover, the required constitutive models to describe the interaction between different components of the model are explained in detail.
- Many factors, such as the degree of deformation, the properties of the oxide layer, the rate of loading or the applied temperature may play an important role in the development of bonding between metallic components. In this paper, the effects of two influencing factors on bond formation, namely the degree of deformation and the thickness of the oxide layers, are numerically investigated.

To accomplish this, first, the mechanism of joining by plastic deformation is explained in Section 2. In addition, a theoretical model is briefly introduced to describe bond strength evolution. Then, a finite element model to describe the bonding mechanism at the microscale level is presented in Section 3. Additionally, the constitutive models implemented by the authors are summarized. These constitutive models were implemented in the nonlinear finite element code FEAP [8] to describe the interaction between the components of the model. Finally, in Section 4, several numerical examples are presented to demonstrate the capabilities of the introduced model. It is shown how the influencing factors such as the degree of deformation and the thickness of the oxide layer may affect bond strength evolution.

2. Bond strength evolution in cold welding process

The process of joining by plastic deformation is also known as "cold welding process". This process has been investigated experimentally by many researchers (e.g., see [9–11]). For example, Conrad and Rice [12] performed a series of tests to understand the relation between the bond strength and the compression load applied during the joining process. They performed the experiments under ultra-high vacuum conditions on very clean and smooth metal surfaces. According to their findings, under such conditions, the bond strength σ_B is almost equal to the normal stress p_n (i.e. pressure) applied to the surfaces participating in joining. That is:

$$\sigma_B \sim p_n \tag{1}$$

However, as explained before, the surface of a metal in atmospheric conditions is always covered by a thin layer of oxide and other contaminants. Fig. 1 is a schematic representation for the bonding process in the presence of oxide layers. The brittle oxide layers above the metallic surfaces can break up when the metals experience large plastic deformations under a high normal pressure. The fracturing of oxide layers creates open spaces between the oxide fragments. Then, the clean metal substrate is able to extrude into the cracks and form the bonding. However, the effective bonding area established along the joint interface is just a fraction of the total area. Therefore, to satisfy the macroscopic force equilibrium, the obtained bond strength has to be proportional to the applied pressure through a surface expansion factor ψ as follows:
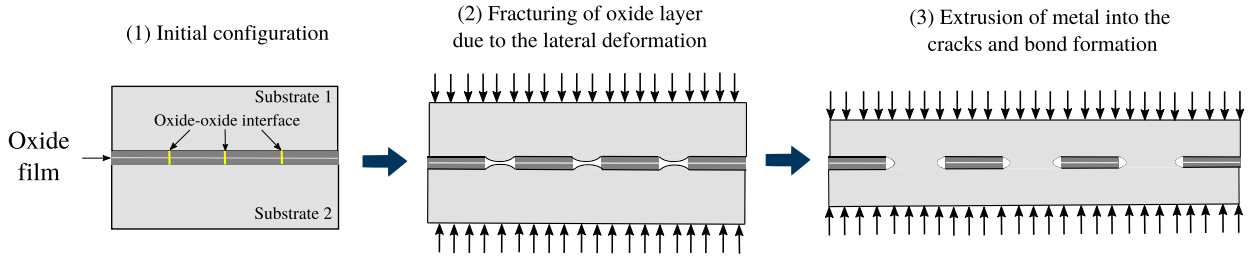
$$\sigma_B = \psi \, p_n \tag{2}$$

Fig. 2. Simplified geometry for the bond formation between two metallic layers subjected to a large plastic deformation.
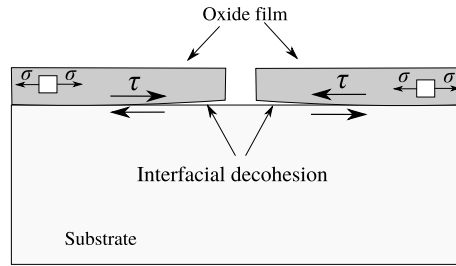

Fig. 3. The decohesion process taking place along the oxide–substrate interface [13].

The surface expansion factor indicates the effective area of bonding along the joint interface. Theoretically, the value of ψ may range from 0 to 1, depending on the degree of deformation along the joint interface. Eq. (2) is the basic equation for bond strength evolution in joining by plastic deformation. This means, having determined the surface expansion ψ and the normal stress p_n, that the bond strength can be estimated by using Eq. (2). The surface expansion ψ is defined as the ratio between the area of the uncovered metal to the total surface area of the joint interface. The surface expansion ψ is given by

$$\psi = \frac{A - A_0}{A} \tag{3}$$

where A_0 and A are the areas of the joint interface for undeformed and deformed configurations, respectively. Under the condition of plane strain, the surface expansion factor can be described through the elongation of the joint interface as follows:

$$\psi = \frac{L - L_0}{L} \tag{4}$$

Here, as illustrated in Fig. 1, L_0 and L are the lengths of the joint interface in their undeformed and deformed configurations, respectively. The surface expansion factor ψ is therefore a quantity allowing one to characterize the degree of deformation. In the following section, a numerical model is presented to simulate bond formation at the microscale level. In this context, the contact pressure and the surface expansion factor are calculated using finite element modeling. Finally, based on these two quantities, bond strength evolution is obtained.

3. Finite element modeling of the joining process at the microscale level

3.1. Description of the model

The objective of this numerical simulation is to describe the microscopic processes taking place when bonding is formed between two metallic layers subjected to large plastic deformations. To this end, the film theory explained in Section 2 is first simplified as shown in Fig. 2. As it is seen in this figure, both metal substrates are covered by a thin layer of oxide. Each oxide layer consists of several segments connected to each other through the oxide–oxide interfaces. For the sake of simplicity, each oxide fragment is modeled as a rectangular block. During the joining process, the substrates may experience large plastic deformations, when they are pressed together. Under such conditions, cracking occurs along the oxide–oxide interfaces. As the cracks are opened, the metal substrates have the possibility to extrude into the open spaces between the oxide fragments and establish bonding. However, before metal extrusion, the existing bonding between the oxide layer and the metal substrate has to be broken. The decohesioning process occurring along the oxide–substrate interface is another important physical phenomenon that has been considered in this study. The decohesioning between the oxide layer and the substrate is due to the generated shear forces along the oxide–substrate interface. This process is shown in Fig. 3.
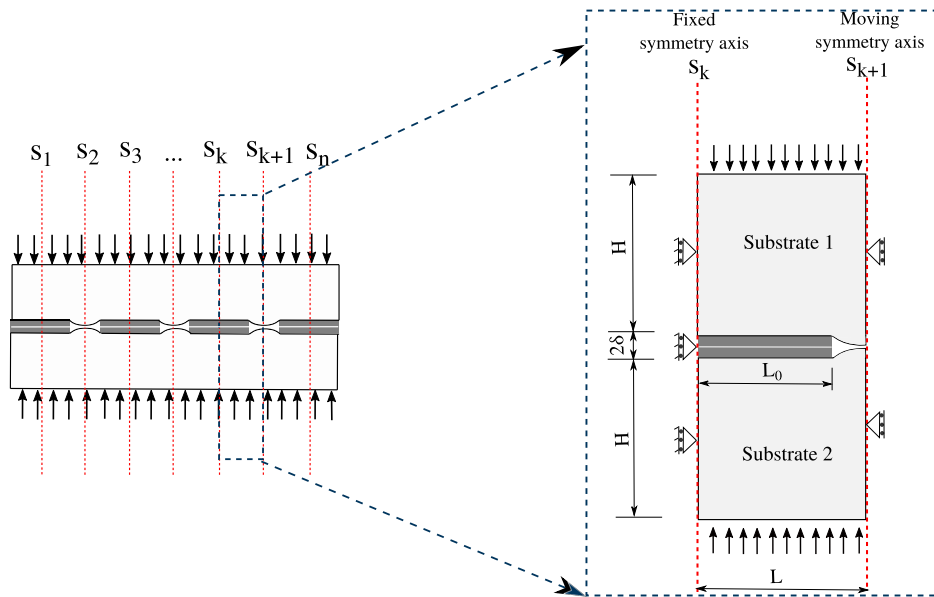
Fig. 4. Geometry and boundary conditions of the finite element model.

Finally, when the two opposing bulk metals come into contact, bonding is established along the substrate–substrate interface. The simplified model shown in Fig. 2 consists of a chain of oxide fragments with a repetitive pattern. As depicted in Fig. 4, many symmetry lines, i.e. $S_1, S_2, \ldots, S_n$, can be defined for the model. Therefore, it would be computationally more efficient to analyze only half of the cracked oxide segment located between the symmetry lines S_k and S_{k+1}. The geometry of the model and the applied boundary conditions are shown in Fig. 4. It should be noted that the model is constraint in x-direction along the line S_k, while, the symmetry line S_{k+1} can move in x-direction. This has been achieved by linking together the x-displacement of all nodes along the axis S_{k+1}. In other words, all the nodes along this axis have the same x-displacement value. The substrates have initially a height of H_0 and a width of L_0. However, after the joining process, their height reduces to H and their width increases to L. The deformation is calculated based on the plane strain condition. In addition, it is assumed that the oxide fragments are much stiffer than the metal substrates. Therefore, the lateral deformation of the oxide blocks can be neglected. The metal substrates show both elasto-plastic behavior with isotropic hardening. A von Mises plasticity model has been employed to describe the mechanical behavior of the metals. The plastic yield function is given by

$$\phi_{\mathrm{p}} = \|\boldsymbol{\sigma}^{\mathrm{dev}}\| - \sqrt{\frac{2}{3}}(\sigma_{\mathrm{Y}} + H_{\mathrm{p}}\varepsilon_{\mathrm{eq}}^{p}) \tag{5}$$

where $\varepsilon_{\mathrm{eq}}^{p}$ is the equivalent plastic strain, $\boldsymbol{\sigma}^{\mathrm{dev}}$ the deviatoric part of the Cauchy stress tensor, σ_{Y} the initial yield stress, and H_{p} represents the isotropic hardening modulus.

It is important to note that, because of the large deformations occurring during the joining process, it is inevitable to use a geometrically non-linear formulation in the presented finite element model. Therefore, the finite element calculations in this study are geometrically non-linear. In order to model the horizontal contact between the two oxide layers, the existing contact model in FEAP has been employed (for more details, see [14]). Other interfaces introduced between the components of the model, i.e. (1) the oxide–oxide interface, (2) the oxide–substrate interface, and (3) the substrate–substrate interface, are shown in Fig. 5.

However, in order to characterize the bonding and debonding processes in this numerical example, it is required to introduce user-defined constitutive models. In this numerical analysis, two models implemented by the authors have been employed to describe the interactions between different components of the model. The user-defined models in this paper are as follows.

- A bilinear cohesive zone model to describe the behavior of both the oxide–substrate and the oxide–oxide interfaces. This model has been included in a zero-thickness interface element to represent both the interfacial decohesion process occurring between the oxide layer and the substrate, and the fracturing of the oxide layer itself.
- An extended version of the bilinear cohesive zone model to describe both bonding and debonding processes along the substrate–substrate interface. This model is essentially a cohesive zone model that accounts for the development of bonding as well.

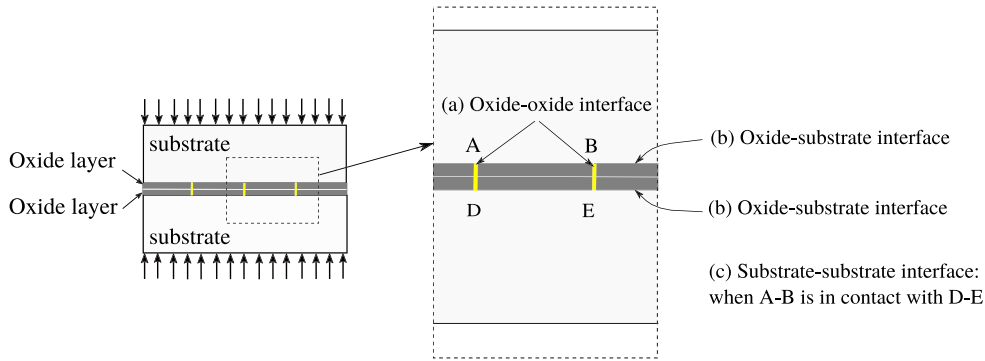The following sections describe the above-mentioned models in more detail.

Fig. 5. The introduced interfaces between the components of the model, i.e. (a) the oxide–oxide interface, (b) the oxide–substrate interface, and (c) the substrate–substrate interface.
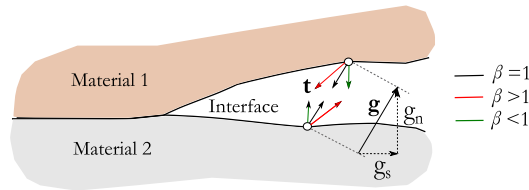

Fig. 6. An interface between two materials with a gap vector **g** and a traction vector **t** between two points; note the influence of the parameter β on the traction vector.

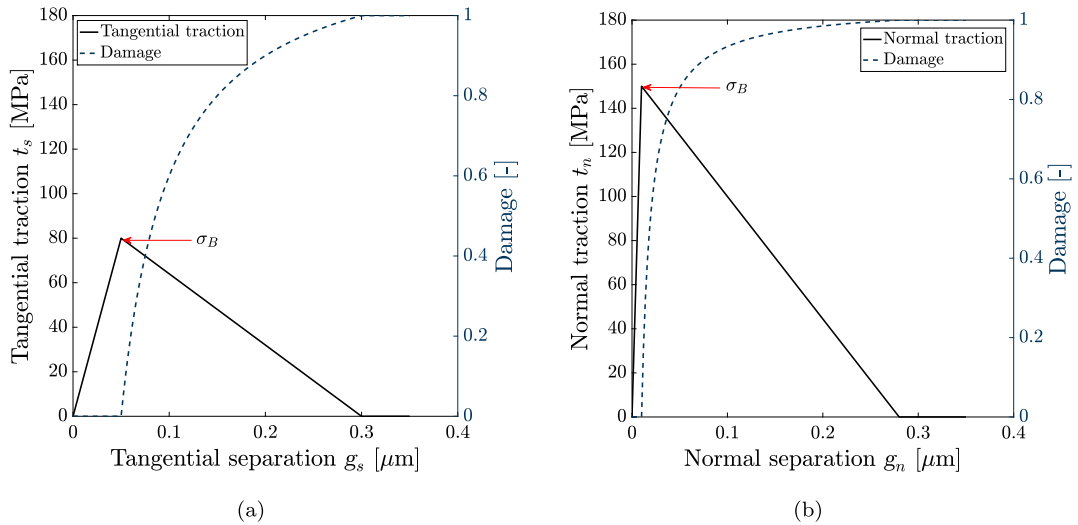### 3.2. Modeling of the oxide–oxide and substrate–oxide behavior

In this paper, a cohesive zone model is employed to describe both the fracturing of the oxide layers and the decohesioning along the substrate–oxide interface. During the recent decades, cohesive zone modeling has been recognized as a powerful tool for describing the non-linear fracture in different engineering applications. These applications cover several engineering fields such as modeling of crack growth in composite materials [15,16], modeling of crystal-coating interface degradation [17], modeling of delamination processes with fiber bridging [18,19], modeling of cracking in rock joints [20] or fiber-reinforced concrete [21]. In general, the cohesive zone method provides a relation between the traction vector $\mathbf{t} = (t_n, t_s)$ and the gap vector $\mathbf{g} = (g_n, g_s)$ within the interface. The gap vector is a quantity that represents the relative displacement between two points on both sides of the interface. Fig. 6 is a schematic representation of these vectors. Depending on the modeling requirements, numerous definitions have been suggested in the literature to describe the traction-separation relation. Among them, bi-linear, tri-linear, polynomial, and exponential models are worth to be mentioned (e.g., see [22]). In this paper, a bi-linear cohesive zone model introduced in Rezaei et al. (2017) [23] has been applied to describe the fracturing of the oxide layer as well as the interfacial decohesion along the substrate–oxide interface. Based on this model, the traction between two layers that are connected through an interface increases linearly by increasing the interfacial separation. However, when the separation across the interface is larger than a threshold value, the traction starts to reduce because of the growth of damage along the interface. Therefore, further separation results in the strength reduction of the interface. Finally, when damage reaches its maximum value, the traction becomes zero, indicating complete separation. Accordingly, the traction–separation law for the applied cohesive zone model is given by

$$t_n = (1 - d)\, k_0 \langle g_n \rangle \tag{6}$$

$$t_s = (1 - d)\, k_0\, g_s\, \beta^2 \tag{7}$$

where g_n and g_s are the normal and tangential components of the gap vector along the interface, respectively. The gap vector $\mathbf{g} = (g_n, g_s)$ is defined based on the relative displacement between the two bodies Ω_1 and Ω_2, as illustrated in Fig. 6. Moreover, t_n and t_s indicate the normal and tangential components of the traction vector. In addition, k_0 and d are the interface stiffness and the damage variable, respectively. The parameter β is a scalar that controls the contribution of the shear components in the traction vector. Fig. 6 shows how the traction vector may change using different values of β. The damage evolution in this model is related to the effective separation λ as follows:

$$d = \begin{cases} 0, & \lambda < \lambda_0 \\ \frac{\lambda_f}{\lambda_f - \lambda_0} \frac{\lambda - \lambda_0}{\lambda}, & \lambda_0 < \lambda < \lambda_f \\ 1, & \lambda_f < \lambda \end{cases} \tag{8}$$

(a)

(b)

Fig. 7. (a) The bilinear traction–separation law for the oxide–substrate interface and the evolution of damage with respect to the tangential separation g_s; (b) the bilinear traction–separation law for the oxide–oxide interface and the evolution of damage with respect to the normal separation g_n.

Here, λ represents the effective separation, λ_0 indicates the threshold for damage initiation, and λ_f is the value of effective separation at which the complete decohesioning takes place. Both λ_0 and λ_f are material parameters of the model. The effective traction t^{cz} and the effective separation λ can be defined by

$$t^{cz} = \sqrt{t_n^2 + \beta^{-2} t_s^2} = (1 - d) k_0 \lambda \tag{9}$$

$$\lambda = \sqrt{\langle g_n \rangle^2 + \beta^2 g_s^2} \tag{10}$$

respectively. In the presented finite element model, the cracking along the oxide–oxide interface is caused by the normal separation (i.e. $g_s = 0$, $\lambda = g_n$, $\beta = 1$), whereas the interfacial decohesion along the oxide–substrate interface is due to tangential separation (i.e. $g_n = 0$, $\lambda = g_s$, $\beta = 1$). Figs. 7a and 7b represent the traction–separation relation for the oxide–substrate interface and the oxide–oxide interface, respectively. As seen in both cases, the traction has a maximum indicated by σ_B. This quantity is a material parameter for the cohesive zone model that shows the maximum achievable traction within the interface before the initiation of damage.

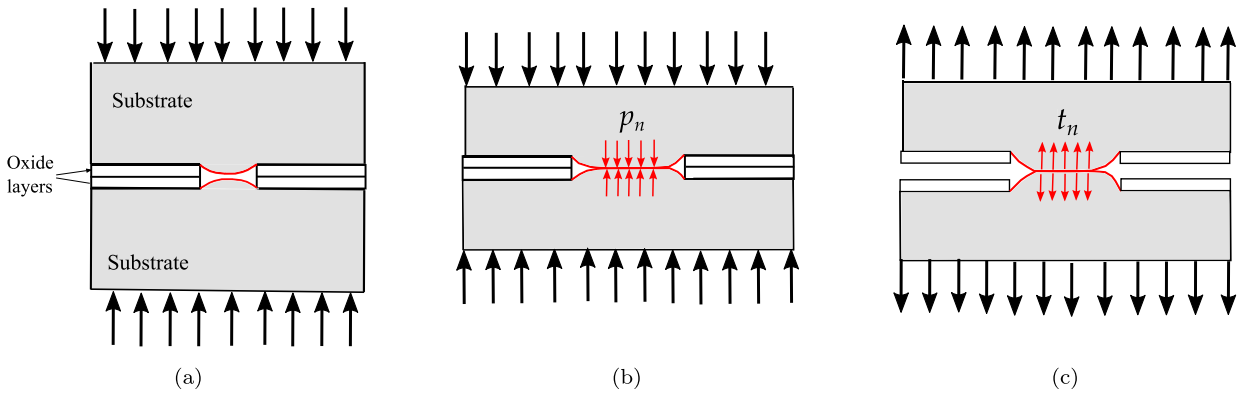### 3.3. Modeling of the substrate–substrate behavior

In this section, bond formation along the substrate–substrate interface is modeled using an extended version of the introduced cohesive zone model. The cohesive zone model introduced in the previous section describes only the process of debonding. This means that it is assumed that the interface introduced between the two surfaces has already a defined bond strength (i.e. $\sigma_B > 0$). Therefore, it shows a resistance force against separation. In this section, the cohesive zone model is modified, such that it accounts for the development of bonding between the two substrates. To achieve this goal, it is assumed that the substrate–substrate interface has initially no resistance against separation (i.e. $\sigma_B = 0$). When the two surfaces come into contact between the cracked oxide segments, the normal pressure increases along their contact area. Therefore, this quantity can contribute to the creation of bonding according to the explanations given in Section 2. In the following, the modeling of bond formation is explained in a systematic manner. The following subsections explain the behavior of the interface in three possible situations, namely (1) before contact, (2) during contact, and (3) during separation.

3.3.1. Substrate–substrate interface before contact

Fig. 8a shows two substrates with no initial contact because of the presence of the oxide layers. A cohesive zone model with zero bond strength is assigned to the interface between the two substrates along their possible contact areas. Since the initial value of bond strength σ_B is equal to zero, the defined interface does not play any role in the development of stress and strain inside the two substrates. In other words, there is no direct interaction between the two substrates. Thus, based on the traction–separation law, the parameter k_0 in Eqs. (6) and (7) becomes zero. That is:

$$k_0 = \frac{\sigma_B}{\lambda_0} = 0 \tag{11}$$

To determine the contact between the two substrates, the normal distance between the opposing nodes of the defined interface element has to be checked. When this distance is zero, the contact is initiated.

Fig. 8. Three possible situations encountered in the modeling of the substrate–substrate interface, (a) before contact (no contact pressure between the two substrates, i.e. $p_n = 0$); (b) under compression (the contact pressure p_n increases along the contact area using Eq. (12) and the bonding is established); (c) during separation (the bonding has been established, the substrate–substrate interface shows the traction t_n).

3.3.2. Substrate–substrate interface during compression

Fig. 8b shows a situation in which the two metal substrates have extruded into the cracked oxide layer. Under such conditions, the virgin substrates come into contact and the normal distance between the surfaces along the contact area becomes zero. Therefore, the interface is activated along the contact area. When the substrates are pressed together, a contact pressure is developed between the bulk metals. In this paper, the contact pressure in normal direction is defined through an empirical hyperbolic model for the pressure–overclosure relationship, as follows [20]:

$$p_\mathrm{n} = k_\mathrm{p} \frac{e \langle -g_\mathrm{n} \rangle}{e + \langle -g_\mathrm{n} \rangle} \tag{12}$$

Here, $\langle x \rangle = (x + |x|)/2$ is the Macauley bracket, k_p indicates a penalty factor and e is a negative input parameter, which shows the maximum allowable value for overclosure $\langle -g_\mathrm{n} \rangle$. The values of k_p and e have to be selected so that, on the one hand, overclosure $\langle -g_\mathrm{n} \rangle$ remains sufficiently small in comparison to the size of the model (i.e. negligible penetration) and, on the other hand, convergence problems are avoided.

Another important step during compression time is to update the bond strength value along the substrate–substrate interface. To this end, the value of the bond strength σ_B is calculated using the explanations given in Section 2. Since the contact has been established between the virgin metals, the bond strength σ_B is equal to the maximum normal stress p_n applied to the surfaces during the compression time [12]. That is:

$$\sigma_\mathrm{B} = p_\mathrm{n} \tag{13}$$

3.3.3. Substrate–substrate interface during separation

Fig. 8c shows a situation in which the substrates are subjected to tensile forces. If the bonding is not formed during the compression time, the bond strength is still zero along the substrate–substrate interface. Therefore, the metallic layers are separated from each other without any resisting force from the interface. However, if bonding is established, the value of the bond strength σ_B is not zero anymore. Therefore, the parameter k_0 in Eqs. (6) and (7) takes a positive value (i.e. $k_0 = \sigma_\mathrm{B}/\lambda_0 > 0$). In this case, the behavior of the substrate–substrate interface is controlled by a bilinear cohesive zone model, as explained before.

4. Results and discussion

For the sake of simplicity, it is assumed that two similar metals are supposed to be joined. In general, the model can be applied to dissimilar metals as well. However, in case of dissimilar metals, the number of material parameters is doubled. The initial thickness of each metal substrate in this numerical example is $H_0 = 10$ μm. Its initial length is assumed to be $L_0 = 5$ μm. Moreover, each oxide layer has a thickness of $\delta = 0.5$ μm. In reality, the oxide fragment length and the fracturing pattern in the oxide layer are not arbitrary. The oxide fragment length might be a function of different factors, such as (1) the degree of surface expansion (or strain), (2) the tensile strength of the oxide layer, (3) the thickness of the oxide layer, (4) the shear strength of the oxide/metal interface, and (5) the presence of local defects. Any changes in these factors may affect the crack density within the brittle oxide layer. Subsequently, the crack spacing and the pressure required for the micro-extrusion of the metal are affected by these changes. During the recent decades, numerous experimental and theoretical studies have been conducted to understand the mechanism of crack growth in coatings at the microscale (e.g., see [24,25]). Moreover, a number of analytical and numerical analyses can be found in the literature to predict the length of fragments and the crack spacing (e.g., see [26,27]). However, in this paper, a predetermined size is assumed for the

Table 1

Material parameters used in the numerical example for modeling the bulk material.

	E [GPa]	ν [–]	σ_Y [MPa]	H_p [MPa]
Oxide film	200	0.3	400	0
Metal substrate	59	0.3	130	50

Table 2

Material parameters used in the numerical example for the interfaces.

Oxide–oxide interface			Oxide–substrate interface			Substrate–substrate interface			
λ_0 [µm]	σ_B [MPa]	λ_f [µm]	λ_0 [µm]	σ_B [MPa]	λ_f [µm]	λ_0 [µm]	k_p [MPa]	λ_f [µm]	e [µm]
0.01	150	0.27	0.05	80	0.3	0.01	10^5	0.2	−0.05

oxide fragment and the focus lies especially on the modeling of micro-mechanisms taking place during the bond formation process. A promising solution to overcome this deficiency is to apply the modeling approach suggested by the authors in [28]. This approach has been essentially developed to predict the fracturing mechanisms in hard coatings. In this method, the coating layer consists of several small grains surrounded by randomly distributed cohesive zone elements. In this way, depending on the loading conditions and the material properties of both coating and substrate, the cracking pattern and the size of fragments can be estimated, and the most probable crack paths can be identified. Nevertheless, this approach is out of the scope of the present paper. The material parameters related to the bulk material and the defined interfaces are shown in Tables 1 and 2, respectively. This numerical simulation consists of two main steps, i.e. (1) the modeling of bond formation under compressive loading, and (2) the modeling of debonding under tensile loading. During the first step, the two metallic substrates are pressed together by applying the predefined vertical displacements to the both ends of the model. Fig. 9 shows the contour plot of the normal stress during the compression time when the thickness of each substrate reduces from 10 µm to 4 µm. During the first stages of the simulation, the damage parameter increases rapidly along the oxide–oxide interface because of the induced lateral deformation. When the damage parameter in the oxide–oxide interface reaches its maximum value, the interface can not carry the stresses anymore. Therefore, cracking occurs along this interface. The complete decohesioning of the oxide–oxide interface is experienced at a surface expansion of almost 5%. Fig. 9a is related to the first stages of the simulation, in which oxide–oxide bonding has been already broken. As the compressive loading continues, the space between the fractured oxide segments increases, and the metal substrates have the possibility to extrude into the created crack. At the same time, decohesioning takes place along the oxide–substrate interface. The process of interfacial decohesion between the oxide and the substrates starts from the edge of the oxide fragment and moves toward its center line during the compression time. This step is shown in Fig. 9b. The extrusion of metal into the created crack and the delamination process along the oxide–substrate interface have been demonstrated in Fig. 10 as well. In this figure, the displacement vectors are plotted. As it is seen, there is a relative tangential displacement between the oxide and the substrates close to the edge of the oxide fragment, indicating interfacial decohesioning. Finally, as shown in Fig. 9c, the metal substrates come into contact after a certain level of compression (about a surface expansion of 20% in this example). By continuing the deformation, the normal stress (i.e. pressure) increases along the substrate–substrate contact area, which indicates the formation of bonding. Fig. 9d shows the last step of the compression, in which the thickness of the metal substrates has reduced to 4 µm (i.e. equal to a surface expansion of almost 60%). In this example, bonding has been successfully established between the two layers. The second step of the simulation deals with the modeling of debonding under tensile loading. In this step, the bonded metallic layers are separated as shown in Fig. 11. This figure shows how debonding takes place between the already bonded metals. By applying a tensile load, debonding develops along the substrate–substrate interface. At the end, the substrate metals become completely debonded.

4.1. Force–displacement curve during bonding and debonding

In this section, the force applied to the upper boundary of the model is computed and plotted versus the vertical displacement to quantify bond strength formation. The force–displacement relations during the bonding and debonding processes are shown in Fig. 12. As it is observed, first, the compressive force increases linearly from point O to A. The deformation in this stage is purely elastic. Then, at point A, the plastic deformation is initiated. From A to B, the upper boundary of the model experiences a vertical displacement of 6 µm that ends up with a surface expansion of almost 60%. Accordingly, the width of the model increases to $L = 12.5$ µm at the end of the compression step. Assuming a width of 1 m for the model, the compressive force increases significantly to almost $F_{com}^{max} = -1900$ N during the compression time. At the end of this stage, the bonding is successfully established between the metal substrates. From B to C, the metallic layers are elastically unloaded. Therefore, the reaction force reduces to zero. The next step, i.e. from C to D, deals with the modeling of debonding under the tensile loading. In this step, the normal traction force between the bonded metals increases linearly to almost $F_{ten}^{com} = 850$ N. This value corresponds to the bond strength of the joint interface. That is:
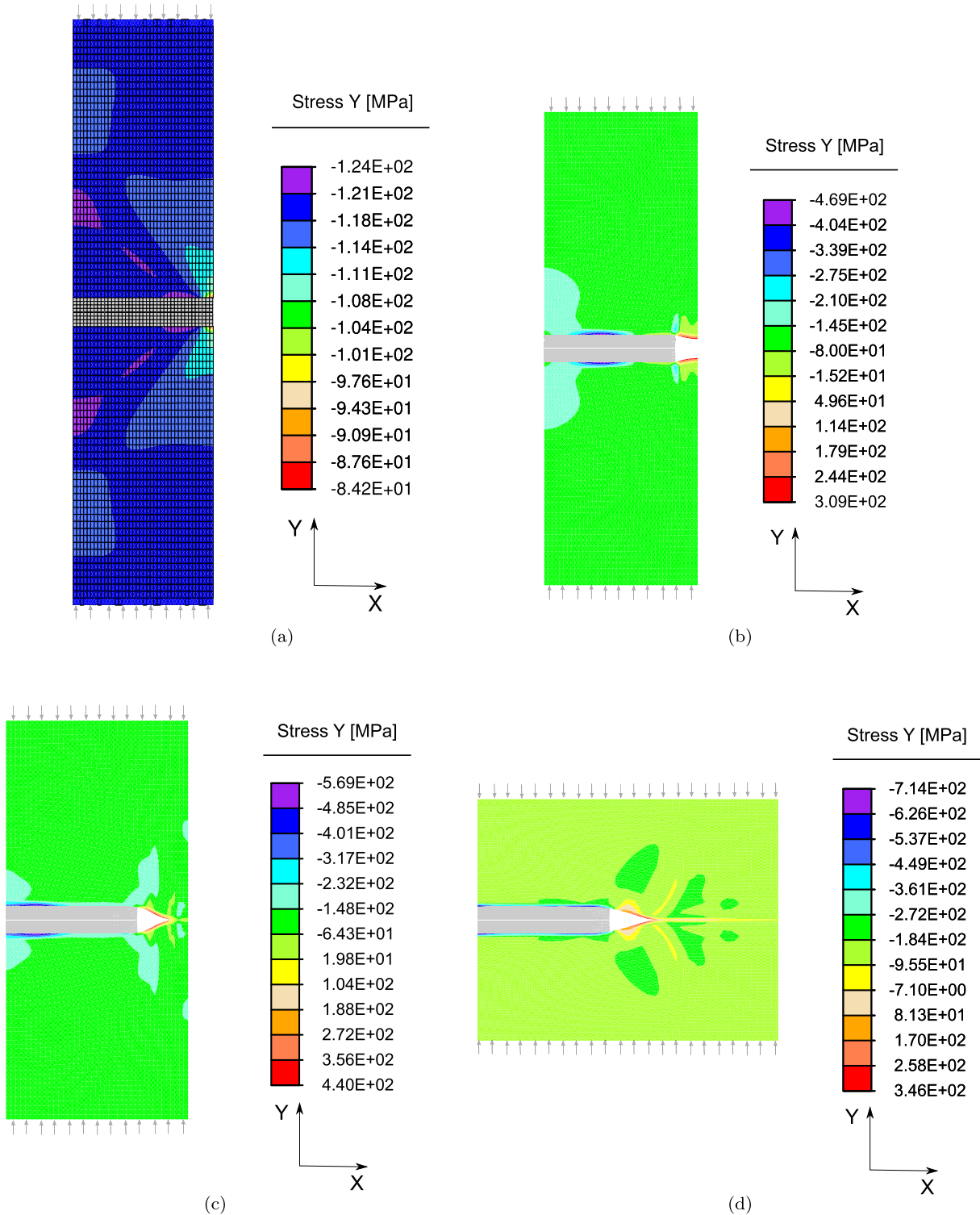
Fig. 9. Modeling of the bonding process at the microscale level: (a) the oxide–oxide interface is debonded, a crack starts to open; (b) the crack is opened and the metal substrate extrude into the crack under the applied pressure; (c) the virgin metals come into contact and the bonding is initiated; (d) the metal substrates are successfully bonded.
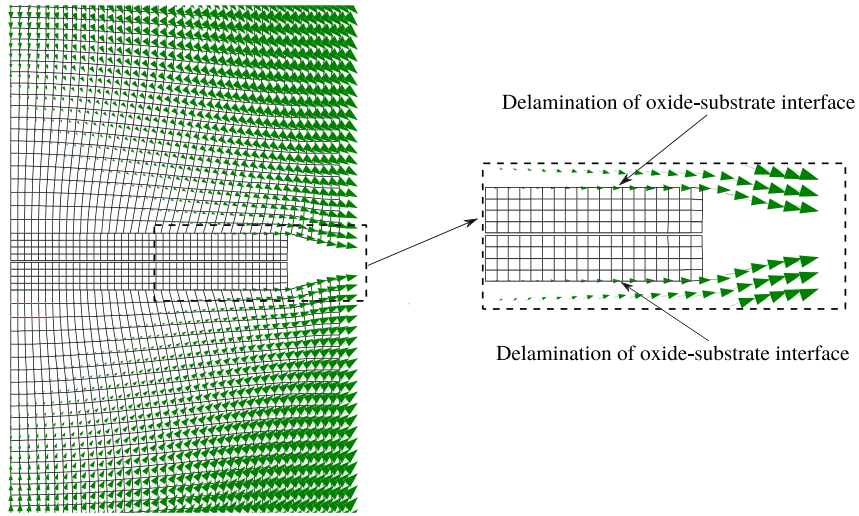
Fig. 10. Extrusion of metal substrates into the created crack and delamination process along the oxide–substrate interface; the arrows indicate the displacement vector.
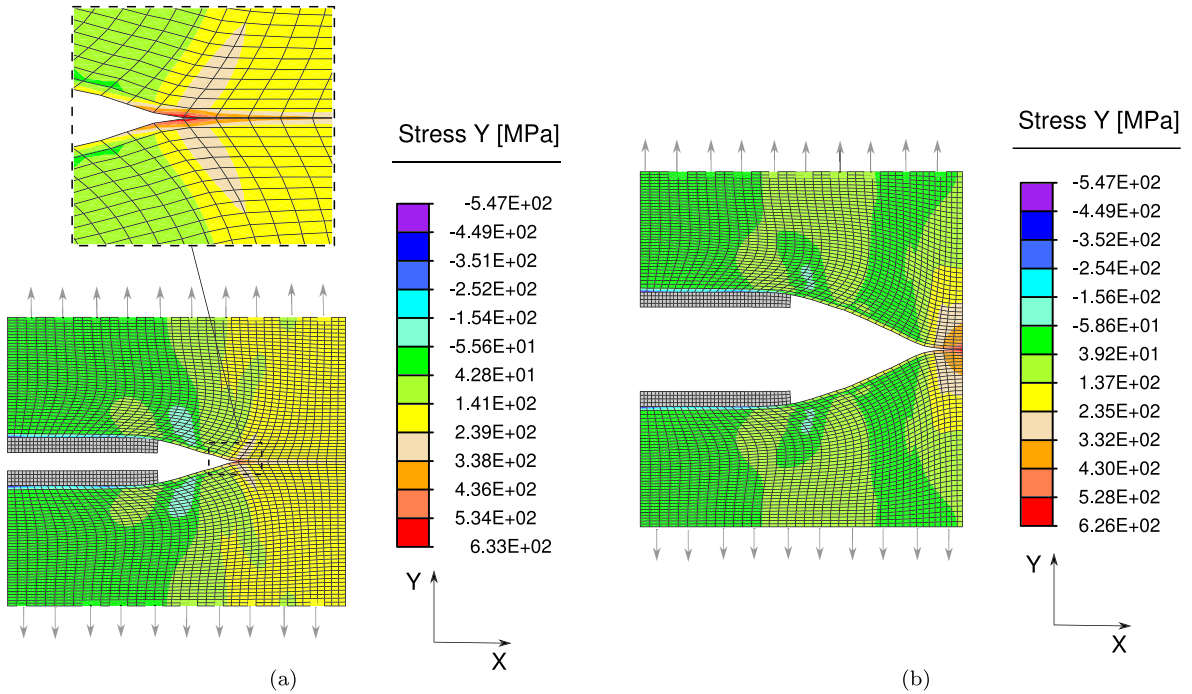
Fig. 11. Modeling of the debonding process under tensile loading: (a) the substrate–substrate interface shows a resistance against separation; (b) debonding has been developed along the substrate–substrate interface.

$$\sigma_{\mathrm{B}} = \frac{F_{\mathrm{ten}}^{\mathrm{max}}}{A} = \frac{850}{12.5\,\mu\mathrm{m} \times 1\,\mathrm{m}} = 68\,[\mathrm{MPa}] \tag{14}$$

However, by increasing the separation, the applied force reduces because of the damage evolution along the substrate–substrate interface. The rate of force reduction increases at point E, because the bonding area reduces rapidly. Finally, at point F, the complete debonding is observed along the substrate–substrate interface.

4.2. Influence of the plastic deformation

In the aforementioned example, the surface expansion of each metal substrate after compression was about 60%. In this section, the effect of this factor on the development of bonding is shown. The surface expansion factor ψ, introduced in Section 2, can be also regarded as a quantity to characterize the degree of deformation. This factor has a significant influence
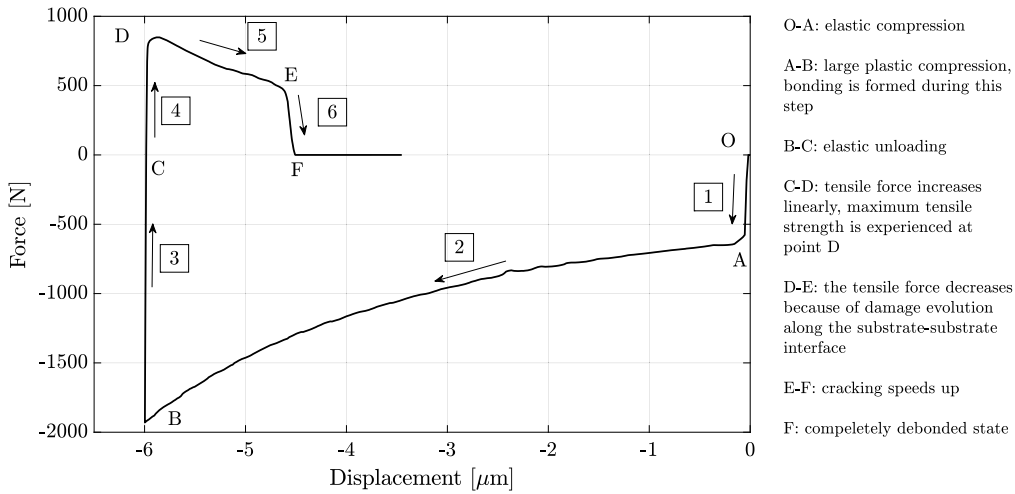
O-A: elastic compression

A-B: large plastic compression, bonding is formed during this step

B-C: elastic unloading

C-D: tensile force increases linearly, maximum tensile strength is experienced at point D

D-E: the tensile force decreases because of damage evolution along the substrate-substrate interface

E-F: cracking speeds up

F: compeletely debonded state

Fig. 12. Force–displacement curve during the bonding and debonding processes.
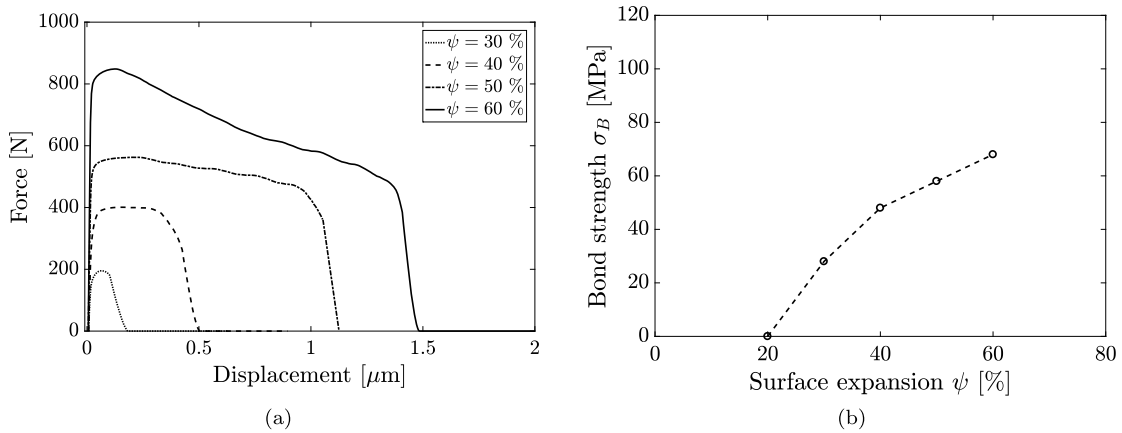

(a)

(b)

Fig. 13. (a) Force–displacement curves during tensile loading for different values of surface expansion; (b) evolution of the bond strength with respect to surface expansion.

on the obtained bond strength. The more the surface expansion takes place, the stronger is the obtained bonding. Higher surface expansions are equivalent to higher plastic deformations within the metallic layers. The influence of the surface expansion factor on bond strength can be observed in Fig. 13a. This figure shows the force–displacement curves during the tensile loading for different values of surface expansion. As it can be seen, the maximum point in these curves increases significantly by increasing the degree of deformation. The evolution of the bond strength after compression with respect to the surface expansion is shown in Fig. 13b. As it is observed, up to a surface expansion of 20%, the bond strength value is zero. This is because the plastic deformation is insufficient for the metal substrates to join together in the created cracks. Therefore, the threshold value of the surface expansion at which the bonding is initiated is about 20% for this numerical example. When surface expansion is larger than the threshold value, the bond strength increases rapidly by increasing plastic deformation.

4.3. Influence of the thickness of the oxide layer

The effect of the surface oxide film on the bond strength can be characterized by its thickness/length ratio (i.e. δ/L_0, see Fig. 4). When this factor increases, more plastic deformation is needed to initiate the bonding between the fractured oxide layers. In other words, this parameter can be regarded as an indicator for the cleanness of the metallic surfaces. In this section, the effect of parameter δ/L_0 on bond formation is investigated. Fig. 14 represents the force–displacement curves during tensile loading considering three different values of δ/L_0, namely 0.1, 0.15 and 0.2. In all three cases, the final surface expansion at the end of the compression process is almost 60%. As seen, the maximum point, which corresponds to the bond strength of the joint interface, reduces significantly by increasing the thickness of the oxide film. As explained before, if the contact surface between metallic layers is not sufficiently clean, bonding may not be established, even if relatively large deformations take place.
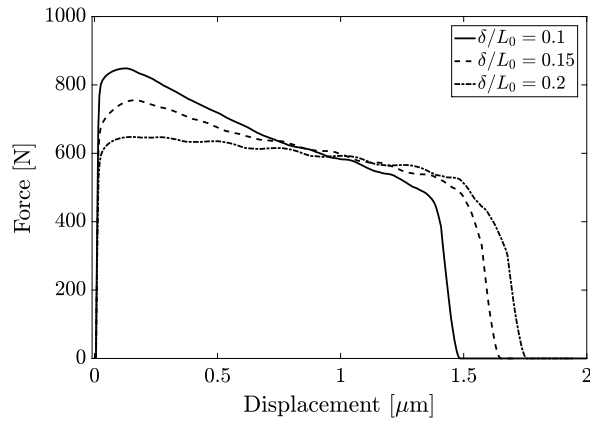
Fig. 14. Force–displacement curves during the tensile loading for different values of δ/L_0.
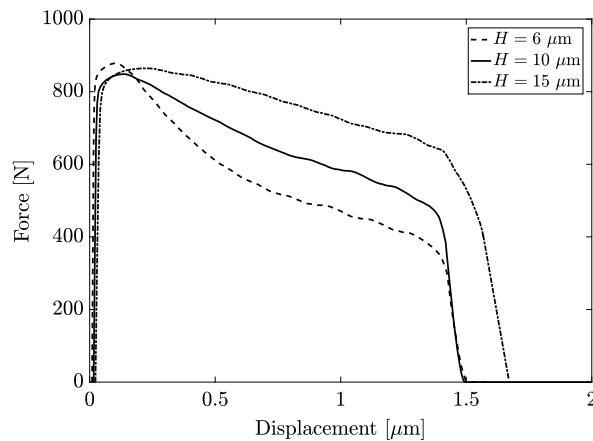

Fig. 15. Force–displacement curves during the tensile loading for different values of H.

4.4. Influence of the substrate thickness

The main challenge in this study is how to define the suitable boundary conditions and the proper dimensions for the model. In this paper, the thickness of the bulk metal is selected such that the local stresses resulting from micro-extrusion do not influence the stress state along the upper boundary of the model. A series of finite element analyses were first performed to find the proper thickness of the substrate. It was found that, when the metal thickness is less than a certain value (about 5 μm in this example), the stresses along the upper boundary are not uniform anymore. On the other hand, by increasing substrate thickness, the number of elements and the computation cost increase. In order to evaluate the effect of metal thickness on the obtained bond strength, different values of the substrate thickness are tested in this section (i.e. $H =$ 6, 10, and 15 μm). The degree of surface expansion ψ and the material properties are similar in all three cases. Fig. 15 shows the force–displacement curves during tensile loading for different substrate thicknesses. As seen, the maximum tensile force required to separate the metals does not change significantly (i.e. it is around 850 N). Therefore, the bond strength σ_B is not affected by the selected thickness if the same values of the surface expansion are applied. However, the post-peak behavior of the curves changes clearly with changing the bulk metal thickness. The reason for this difference is due to the deformation taking place in the bulk metal itself during tensile loading. As the thickness changes, the deformation carried by the bulk metal changes. This can affect the total separation along the interface.

5. Conclusions

In this paper, a finite element model has been developed to describe the metal bonding process at the microscale level. On this basis, the physical mechanisms taking place during the process of joining by plastic deformation have been numerically modeled. Moreover, the constitutive models employed to describe the interfaces between different components of the model were introduced. In the numerical example, the effects of two important factors, such as the degree of deformation and the thickness of the oxide film on bond formation have been investigated. The results of the given numerical examples demonstrate that, during the bonding process, bonding is not obtained until a threshold surface expansion is reached.

Beyond this threshold value, the bond strength increases rapidly with increasing the plastic deformation. In addition, insufficient surface expansion and surface cleanness may result in unsuccessful bonding. The finite element model introduced in this paper may be considered as a useful tool to identify the key parameters affecting the bond formations.

Acknowledgements

References

[1] N. Bay, Cold welding. Part 1: characteristics, bonding mechanisms, bond strength, Met. Constr. (1986) 369–372.

[2] W. Zhang, N. Bay, Cold welding—theoretical modeling of the weld formation, Weld. J. 76 (10) (1997) 417–430.

[3] D.R. Cooper, J.M. Allwood, The influence of deformation conditions in solid-state aluminium welding processes on the resulting weld strength, J. Mater. Process. Technol. 214 (11) (2014) 2576–2592.

[4] M. Bambach, M. Pietryga, A. Mikloweit, G. Hirt, A finite element framework for the evolution of bond strength in joining-by-forming processes, J. Mater. Process. Technol. 214 (10) (2014) 2156–2168.

[5] W. Zhang, N. Bay, Cold welding: experimental investigation of the surface preparation methods, Weld. J. 76 (8) (1997) 326–330.

[6] R. Kebriaei, I. Vladimirov, S. Reese, Joining of the alloys AA1050 and AA5754—experimental characterization and multiscale modeling based on a cohesive zone element technique, J. Mater. Process. Technol. 214 (10) (2014) 2146–2155.

[7] N. Bay, Mechanisms producing metallic bonds in cold welding, Weld. J. 62 (5) (1983) 137–141.

[8] R.L. Taylor, FEAP—A Finite Element Analysis Program, Version 8.4 Theory Manual, Department of Civil and Environmental Engineering University of California at Berkeley, USA.

[9] C. Clemensen, O. Juelstorp, N. Bay, Cold welding. Part 3: influence of surface preparation on bond strength, Met. Constr. (1986) 625–629.

[10] R. Jamaati, S. Amirkhanlou, M.R. Toroghinejad, B. Niroumand, Significant improvement of semi-solid microstructure and mechanical properties of A356 alloy by ARB process, Mater. Sci. Eng., A 528 (6) (2011) 2495–2501.

[11] P. Groche, S. Wohletz, A. Erbe, A. Altin, Effect of the primary heat treatment on the bond formation in cold welding of aluminum and steel by cold forging, J. Mater. Process. Technol. 214 (10) (2014) 2040–2048.

[12] H. Conrad, L. Rice, The cohesion of previously fractured fcc metals in ultrahigh vacuum, Metall. Mater. Trans., B 1 (11) (1970) 3019–3029.

[13] C. Xie, W. Tong, Cracking and decohesion of a thin Al_2O_3 film on a ductile Al–5% Mg substrate, Acta Mater. 53 (2) (2005) 477–485.

[14] R.L. Taylor, G. Zavarise, FEAP—A Finite Element Analysis Program, Version 8.4 Contact Programmer Manual, Department of Civil and Environmental Engineering University of California at Berkeley, USA.

[15] G. Alfano, M.A. Crisfield, Finite element interface models for the delamination analysis of laminated composites: mechanical and computational issues, Int. J. Numer. Methods Eng. 50 (7) (2001) 1701–1736.

[16] H. Li, N. Chandra, Analysis of crack growth and crack-tip plasticity in ductile materials using cohesive zone models, Int. J. Plast. 19 (6) (2003) 849–882.

[17] S. Wulfinghoff, A generalized cohesive zone model and a grain boundary yield criterion for gradient plasticity derived from surface-and interface-related arguments, Int. J. Plast. 92 (2017) 57–78.

[18] D. Höwer, B.A. Lerch, B.A. Bednarcyk, E.J. Pineda, S. Reese, J.-W. Simon, Cohesive zone modeling for mode i facesheet to core delamination of sandwich panels accounting for fiber bridging, Compos. Struct. (2017), https://doi.org/10.1016/j.compstruct.2017.07.005.

[19] M. Heidari-Rarani, M. Shokrieh, P. Camanho, Finite element modeling of mode I delamination growth in laminated DCB specimens with R-curve effects, Composites, Part B, Eng. 45 (1) (2012) 897–903.

[20] A. Pouya, P.B. Yazdi, A damage-plasticity model for cohesive fractures, Int. J. Rock Mech. Min. Sci. 73 (2015) 194–202.

[21] K. Park, K. Ha, H. Choi, C. Lee, Prediction of interfacial fracture between concrete and fiber reinforced polymer (FRP) by using cohesive zone modeling, Cem. Concr. Compos. 63 (2015) 122–131.

[22] K. Park, G.H. Paulino, Cohesive zone models: a critical review of traction–separation relationships across fracture surfaces, Appl. Mech. Rev. 64 (6) (2011) 060802.

[23] S. Rezaei, S. Wulfinghoff, S. Reese, Prediction of fracture and damage in micro/nano coating systems using cohesive zone elements, Int. J. Solids Struct. 121 (2017) 62–74, https://doi.org/10.1016/j.ijsolstr.2017.05.016.

[24] D.C. Agrawal, R. Raj, Measurement of the ultimate shear strength of a metal–ceramic interface, Acta Metall. 37 (4) (1989) 1265–1270.

[25] M. Nagl, S. Saunders, W. Evans, D. Hall, The tensile failure of nickel oxide scales at ambient and at growth temperature, Corros. Sci. 35 (5–8) (1993) 965971–969977.

[26] B. Picqué, P.-O. Bouchard, P. Montmitonnet, M. Picard, Mechanical behaviour of iron oxide scale: experimental and numerical study, Wear 260 (3) (2006) 231–242.

[27] A. Taylor, V. Edlmayr, M. Cordill, G. Dehm, The effect of film thickness variations in periodic cracking: analysis and experiments, Surf. Coat. Technol. 206 (7) (2011) 1830–1836.

[28] S. Rezaei, M. Arghavani, S. Wulfinghoff, N.C. Kruppe, T. Brögelmann, S. Reese, K. Bobzin, A novel approach for the prediction of deformation and fracture in hard coatings: comparison of numerical modeling and nanoindentation tests, Mech. Mater. 117 (2018) 192–201, https://doi.org/10.1016/j.mechmat.2017.11.006.